

# Photonic-crystal membranes for optical detection of single nano-particles, designed for biosensor application

Jon Olav Grepstad,<sup>1,2,3,\*</sup> Peter Kaspar,<sup>4</sup> Olav Solgaard,<sup>5</sup> Ib-Rune Johansen,<sup>2</sup> and Aasmund S. Sudbø<sup>6,3</sup>

<sup>1</sup>*Department of Electronics and Telecommunications, Norwegian University of Science and Technology, NO-7491 Trondheim, Norway*

<sup>2</sup>*SINTEF ICT, Microsystems and Nanotechnology, NO-0373, Norway*

<sup>3</sup>*University Graduate Center, NO-2027 Kjeller, Norway*

<sup>4</sup>*Electronics Laboratory, ETH Zurich, CH-8092 Zurich, Switzerland*

<sup>5</sup>*E.L. Ginzton Laboratory, Stanford University, CA-94305, USA*

<sup>6</sup>*Department of Physics, University of Oslo, NO-0316, Norway*

[\\*jonolav.grepstad@sintef.no](mailto:jonolav.grepstad@sintef.no)

**Abstract:** A sensor designed to detect bio-molecules is presented. The sensor exploits a planar 2D photonic crystal (PC) membrane with sub-micron thickness and through holes, to induce high optical fields that allow detection of nano-particles smaller than the diffraction limit of an optical microscope. We report on our design and fabrication of a PC membrane with a nano-particle trapped inside. We have also designed and built an imaging system where an optical microscope and a CCD camera are used to take images of the PC membrane. Results show how the trapped nano-particle appears as a bright spot in the image. In a first experimental realization of the imaging system, single particles with a radius of 75 nm can be detected.

© 2012 Optical Society of America

**OCIS codes:** (220.0220) Optical design and fabrication; (280.4788) Optical sensing and sensors

---

## References and links

1. B. Bohunicky and S. A. Mousa, "Biosensors: the new wave in cancer diagnosis," *Nanotech. Sci. Appl.* **4**, 1–10 (2010).
2. T. Reichlin, W. Hochholzer, S. Bassetti, S. Steuer, C. Stelzig, S. Hartwiger, S. and Biedert, N. Schaub, C. Buerge, M. Potocki, M. Noveanu, T. Breidhardt, R. Twerenbold, K. Winkler, R. Bingisser, and C. Mueller, "Early diagnosis of myocardial infarction with sensitive cardiac troponin assays," *N. Engl. J. Med.* **361**, 858–867 (2009).
3. P. Stefaniuk, J. Cianciara, and A. Wiercinska-Drapalo, "Present and future possibilities for early diagnosis of hepatocellular carcinoma," *World J. Gastroenterol.* **16**, 418–424 (2010).
4. M. F. Pineda, L. L. Chan, T. Kuhlenschmidt, C. J. Choi, M. Kuhlenschmidt, and B. T. Cunningham, "Rapid specific and label-free detection of porcine rotavirus using photonic crystal biosensors," *IEEE Sens. J.* **9**, 470–477 (2009).
5. A. A. Yanik, M. Huang, O. Kamohara, A. Artar, T. W. Geisbert, J. H. Connor, and H. Altug, "An optofluidic nanoplasmonic biosensor for direct detection of live viruses from biological media," *Nano Lett.* **10**, 4962–4969 (2010).
6. Product info: <http://www.axis-shield.com>, visited March 15, 2012.
7. D. W. G. Morrison, M. R. Dokmeci, U. Demirci, and A. Khademhosseini, *Biomedical Nanostructures* (John Wiley & Sons, Inc., 2008). Chap. 17.
8. L. Li, "Recent development of micromachined biosensors," *IEEE Sens. J.* **11**, 305–311 (2011).

9. Y. Cui, Q. Wei, H. Park, and C. M. Lieber, "Nanowire nanosensors for highly sensitive and selective detection of biological and chemical species," *Science* **293**, 1289–1292 (2001).
10. Y. L. Bunimovich, Y. S. Shin, W. Yeo, M. Amori, G. Kwong, and J. R. Heath, "Quantitative real-time measurements of dna hybridization with alkylated nonoxidized silicon nanowires in electrolyte solution," *J. Am. Chem. Soc.* **128**, 16323–16331 (2006).
11. C. A. Savran, S. M. Knudsen, A. D. Ellington, and S. R. Manalis, "Micromechanical detection of proteins using aptamer-based receptor molecules," *Anal. Chem.* **76**, 3194–3198 (2004).
12. J. Fritz, M. K. Baller, H. P. Lang, H. Rothuizen, P. Vettiger, E. Meyer, H. J. Guntherodt, C. Gerber, and J. K. Gimzewski, "Translating biomolecular recognition into nanomechanics," *Science* **288**, 316–318 (2000).
13. A. K. Gupta, P. R. Nair, D. Akin, M. R. Ladisch, S. Broyles, M. A. Alam, and R. Bashir, "Anomalous resonance in a nanomechanical biosensor," *Proc. Natl. Acad. Sci. U. S. A.* **103**, 13362–13367 (2006).
14. E. Stern, R. Wagner, F. J. Sigworth, R. Breaker, T. M. Fahmy, and M. A. Reed, "Importance of the debye screening length on nanowire field effect transistor sensors," *Nano Lett.* **7**, 3405–3409 (2007).
15. J. Lee, K. Icoz, A. Roberts, A. D. Ellington, and C. A. Savran, "Diffractometric detection of proteins using microbead-based rolling circle amplification," *Anal. Chem.* **82**, 197–202 (2010).
16. X. Fan, I. M. White, S. I. Shopova, H. Zhu, J. D. Suter, and Y. Sun, "Sensitive optical biosensors for unlabeled targets: a review," *Anal. Chim. Acta* **620**, 8–26 (2008).
17. F. Hsiao and C. Lee, "Computational study of photonic crystals nano-ring resonator for biochemical sensing," *IEEE Sens. J.* **10**, 1185–1191 (2010).
18. J. G. Ruperez, V. Toccafondo, M. J. Bañuls, J. G. Castelló, A. Griol, S. Peransi-Llopis, and A. Maquieira, "Label-free antibody detection using band edge fringes in soi planar photonic crystal waveguides in the slow-light regime," *Opt. Express* **18**, 24276–24286 (2010).
19. M. R. Lee and P. M. Fauchet, "Nanoscale microcavity sensor for single particle detection," *Opt. Lett.* **32**, 3284–3286 (2007).
20. S. Zlatanovic, L. W. Mirkarimi, M. M. Sigalas, M. A. Bynum, E. Chow, K. M. Robotti, G. W. Burr, S. Esener, and A. Grot, "Photonic crystal microcavity sensor for ultracompact monitoring of reaction kinetics and protein concentration," *Sens. Actuator B* **141**, 13–19 (2009).
21. Q. Quan, I. B. Burgess, S. K. Y. Tang, D. L. Floyd, and M. Loncar, "High-q, low index-contrast polymeric photonic crystal nanobeam cavities," *Opt. Express* **19**, 22191–22197 (2011).
22. S. Lal, S. Link, and N. J. Halas, "Nano-optics from sensing to waveguiding," *Nat. Photonics* **1**, 641–648 (2007).
23. S. W. Bishnoi, C. J. Rozell, C. S. Levin, M. K. Gheith, B. R. Johnson, D. H. Johnson, and N. J. Halas, "All-optical nanoscale ph meter," *Nano Lett.* **6**, 1687–1692 (2006).
24. J. N. Anker, W. P. Hall, O. Lyandres, N. C. Shah, J. Zhao, and R. P. Duynne, "Biosensing with plasmonic nanosensors," *Nat. Mater.* **7**, 442–453 (2008).
25. J. C. Yang, J. Ji, J. M. Hogle, and D. N. Larson, "Multiplexed plasmonic sensing based on small-dimension nanohole arrays and intensity interrogation," *Biosens. Bioelectron.* **24**, 2334–2338 (2009).
26. A. Lesuffleur, H. Im, N.-C. Lindquist, and S. H. Oh, "Periodic nanohole arrays with shape-enhanced plasmon resonance as real-time biosensors," *Appl. Phys. Lett.* **90**, 243110 (2007).
27. M. E. Stewart, N. H. Mack, V. Malyarchuk, J. A. N. T. Soares, T. W. Lee, S. K. Gray, R. G. Nuzzo, and J. A. Rogers, "Quantitative multispectral biosensing and 1d imaging using quasi-3d plasmonic crystals," *Proc. Natl. Acad. Sci. U. S. A.* **103**, 17143–17148 (2006).
28. A. G. Brolo, R. Gordon, B. Leathem, and K. L. Kavanagh, "Surface plasmon sensor based on the enhanced light transmission through arrays of nanoholes in gold films," *Langmuir* **20**, 4813–4815 (2004).
29. M. Kaskar, P. Paddon, V. Pacradouni, R. Morin, A. Busch, J. F. Young, S. R. Johnson, J. MacKenzie, and T. Tiedje, "Observation of leaky slab modes in an air-bridged semiconductor waveguide with a two-dimensional photonic lattice," *Appl. Phys. Lett.* **70**, 1438–1440 (1997).
30. S. Fan and J. D. Joannopoulos, "Analysis of guided resonances in photonic crystal slabs," *Phys. Rev. B* **65**, 235112 (2002).
31. M. E. Beheiry, V. Liu, S. Fan, and O. Levi, "Sensitivity enhancement in photonic crystal slab biosensors," *Opt. Express* **18**, 22702–22714 (2010).
32. Commercially available software supplied by KJ Innovation, <http://software.kjinnovation.com/GD-Calc.html> visited Sept. 15, 2011.
33. Z. Popovic and B. D. Popovic, *Introductory Electromagnetics* (Prentice Hall, Inc., 2000).
34. M. J. Banuls, V. Gonzalez-Pedro, C. A. Barrios, R. Puchades, and A. Maquieira, "Selective chemical modification of silicon nitride/silicon oxide nanostructures to develop label-free biosensors," *Biosens. Bioelectron.* **25**, 1460–1466 (2010).
35. C. F. Bohren and D. R. Huffman, *Absorption and Scattering of Light by Small Particles* (John Wiley and Sons, Inc., 1998). Chap. 5.
36. J. Vrs, "The density and refractive index of adsorbing protein layers," *Biophys. J.* **87**, 553–561 (2004).
37. M. Huang, A. A. Yanik, T. Y. Chang, and H. Altug, "Sub-wavelength nanofluidics in photonic crystal sensors," *Opt. Express* **17**, 24224–24233 (2009).
38. M. G. Hale and M. R. Querry, "Optical constants of water in the 200-nm to 200- $\mu$ m wavelength region," *Appl.*

## 1. Introduction

To make medical diagnosis more efficient and accurate, better instruments for specific detection of common pathogens are needed [1–3]. Accurate monitoring of contamination in sources of water- and food can prevent outbreak of disease [4]. Monitoring biological hazards has also been called for in the combat against bio-terrorism [5]. A solution to these challenges is sensors that can capture and detect very low concentrations of specific proteins, viruses, bacteria, etc., in samples where the concentration of non-targeted substances is many orders of magnitude higher. That is, biosensors with high specificity and sensitivity.

Commercially available instruments fit on a benchtop and detect a number of biological markers. Even hand-held devices are offered. Albumin, C-Reactive protein and lipid detection can be done with a stationary device the size of a shoe box [6], while hand-held glucose, fertility and pregnancy tests, can be bought in general pharmacies. By making sensors efficient, cheap and small, we provide solutions for point-of-care and in-home testing. The use of expensive and time-consuming labs run by professional personnel can hence be avoided.

Micro- and nano-fabrication techniques can in general provide devices that are small, reliable and cheap, and recent developments suggest that the next generation biosensors will be made exploiting this technology [7, 8]. While platforms using electric or mechanical transducers exist [9–12], biochemical sensor platforms with optical readout seem particularly promising. Optical readout provides compatibility with the wet environment presented in a biological system [13, 14], and can also be done without physically interconnecting the light source, transducer and light detector [4, 15].

Some of the most sensitive biosensors with optical readout today are based on dielectric photonic crystals (PCs) [16–21] and nanoplasmonics [22–28]. They all rely on surface chemistry to capture specific target molecules. Specificity is hence mainly provided by chemical means. The sensitivity is limited by transducer design, where the fundamental aim is to maximize the concentration of light where captured target molecules settle.

For dielectric PC sensors, their ability to concentrate light into a very small detection volume has been exploited to demonstrate sensitivities close to a single molecule [19, 20]. However, these schemes have strict alignment requirements, because light must be coupled into single-mode waveguides in order to lead light to the detection volume. Alignment is an expensive, time-consuming process, rendering such sensors unsuitable for point-of-care applications. Sensors based on nanoplasmonics, on the other hand, are tolerant regarding alignment and still show impressive sensitivities [22–28].

In this paper we propose to combine the convenient light coupling found in nanoplasmonic sensors and the high electromagnetic field intensities obtainable in dielectric PCs, in a dielectric PC membrane. PC membranes are in general comprised of a thin slab with a periodic in-plane variation in permittivity. They can in many ways be considered as regular slab waveguides, but in addition to having a series of guided modes, they also exhibit a group of modes called guided resonances [29, 30]. Coupling to guided resonances can be done by normal incidence light, and produces high fields in the membrane [31]. A small particle placed in this field will absorb energy from the guided-resonance mode field. The particle will reradiate the absorbed energy in all directions. An adapted imaging system can then refocus the radiation on a CCD sensor, giving rise to a bright spot in the resulting image.

A novel planar 2D dielectric PC membrane has been developed to demonstrate this detection principle. We present the basic working principle, processing techniques and preliminary results from optical characterization. Detection of a single particle with  $\sim 75$  nm radius is demonstrated.

## 2. Design of photonic crystal membrane and working principle

The basic elements of the sensor are summarized in Fig. 1. At the core of the sensor there is a planar dielectric membrane with through holes. Fig. 1(A) illustrates how the membrane is free-standing, permitting gas or fluid samples to be physically pushed through the holes in the membrane. The optical effect of two nano-particles trapped inside the membrane is illustrated in Fig. 1(B). It has been simplified to illustrate the idea that nano-particles are detected by a CCD camera as bright spots on a dark background. We will further explain how this concept can be realized.

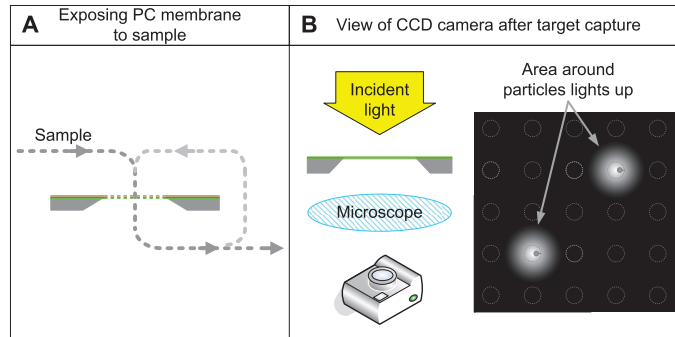


Fig. 1. A summary of how the sensor works. (A) A sample is pumped through the PC membrane and two particles are caught in the membrane holes. (B) Captured particles are detected as bright spots on a dark background by an optical microscope and a CCD-camera.

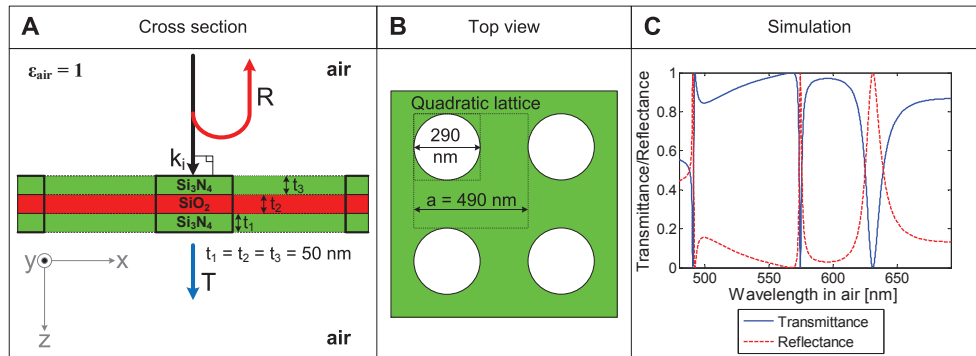


Fig. 2. (A) Cross section and (B) top view of the designed photonic crystal membrane. (C) Simulated transmittance and reflectance for a normal incidence plane wave is given as a function of wavelengths from 490 to 692 nm.

### 2.1. Simulations of perfectly periodic photonic crystal membranes

The current PC membrane is comprised of holes arranged in a square lattice, nominally with period  $a = 490$  nm and radius  $r = 145$  nm. As illustrated in Fig. 2(A) and (B), the holes are etched in a three layered thin-film stack, formed by  $\text{Si}_3\text{N}_4$  and  $\text{SiO}_2$  with nominal thicknesses  $t_1 = t_2 = t_3 = 50$  nm.

The spectral response of the PC membrane, to linearly polarized normal incidence plane waves, has been simulated using rigorously coupled wave analysis (RCWA) in 3D, implemented in a Matlab based simulation software [32]. The spectral bandwidth of the simulation

is bound by:

$$a < \lambda < \sqrt{2}a, \quad (1)$$

where  $a$  is the lattice period and  $\lambda$  is the wavelength in the medium surrounding the membrane. We motivate this choice in the text below.

Plots of transmittance and reflectance as a function of wavelength are given in Fig. 2(C) for the structure in Fig. 2(A) and (B). Asymmetric resonant features, known as Fano lines, appear in the spectrum at 491, 575 and 631 nm. They can be interpreted as a slowly varying response, corresponding to what is found in homogeneous slabs, interfering with three fast varying Lorentzian shaped signals, formed as a result of incoming light coupling to guided resonance modes [30]. Consequently, we expect the electromagnetic field in the membrane to be amplified in the spectral vicinity of the three wavelengths 491, 575 and 631 nm.

Full field simulations, for normal incidence linearly polarized waves, have been performed for the guided resonance mode at 631 nm. Results show how the polarization is approximately conserved. Moreover, light couples to a “TE-like” guided resonance mode field that concentrates in the holes. This is intuitive, since the electromagnetic field is mainly polarized in the membrane plane and the normal component of the electric displacement field must be continuous at air-membrane-boundaries [33]. The field hence concentrates in the holes as a result of permittivity contrast between the membrane materials and the air in the holes. An increase in contrast between air and the membrane material, will in general induce higher electromagnetic fields in the holes. Note that, the complex geometry of three thin films is not chosen based on optical properties. Using this structure, the center layer, inside of holes, is chemically different than the membrane outer surface. In a biosensing application, surface chemistry can hence be used to functionalize the inside of holes to capture target particles, while the membrane outer surface can be passivated [34]. In this way, target particles tend to stick at positions with maximum optical field intensity, ensuring maximal sensitivity.

Requiring  $\lambda > a$ , the discrete translation symmetry in the PC membrane ensures that there are no diffracted waves for normal incidence waves. In that case, the optical response of the PC membrane is particularly simple. There are only two non-evanescent waves to which a normal incidence field can couple: One transmitted and one reflected wave, both with wave vectors normal to the membrane plane. The transmitted and reflected power is bound to the 0<sup>th</sup> order of diffraction.

Placing a particle in the PC membrane breaks the discrete translation symmetry. Power is then no longer bound to the 0<sup>th</sup> order of diffraction, but can appear also in higher diffraction orders. The details of this process are complicated, but can be greatly simplified by considering a particle of limited size. We will consider particles that are so small that the field distribution in the PC membrane is approximately unchanged by the presence of a particle in the membrane. The total optical response, as seen from a detector placed outside the membrane, is then a superposition of the scattered light from the particle on the transmitted and reflected wave.

## 2.2. Rayleigh scattering model for defects

The particle will scatter the field in its location, and as mentioned above, the field is approximately linearly polarized for normal incidence linearly polarized waves. To find the scattered power from the particle, we model the particle as a dielectric sphere with relative permittivity  $\epsilon_p$  surrounded by a medium with permittivity  $\epsilon_m$ , illuminated by a harmonic linearly polarized plane wave with amplitude  $E_p$  and vacuum wavelength  $\lambda$ . The sphere is assumed to be small, i.e.

$$r_p \ll \lambda / (2\pi\sqrt{\epsilon_p}). \quad (2)$$

The sphere will scatter light, radiating a wave similar to that of an ideal dipole, a phenomenon known as Rayleigh scattering [35]. The total scattered power from one single sphere is

$$P_R = \frac{4\pi}{3} \sqrt{\frac{\epsilon_0}{\mu_0}} \left( \frac{2\pi}{\lambda} \right)^4 \left| \frac{\epsilon_p - \epsilon_m}{\epsilon_p + 2\epsilon_m} \right|^2 \epsilon_m^{\frac{5}{2}} r_p^6 E_p^2. \quad (3)$$

In our context, this result is clearly an approximation. When the particle is placed inside a hole in a PC membrane, the induced electric dipole fields from the particle will induce dipoles in the hole wall.  $P_R$  must hence depend on the PC membrane geometry and the particle location. However, if we also impose the condition that  $r_p \ll r$ , where  $r$  is the radius of holes, and place the particle in the middle of a hole, the contribution from the particle dipole to the electric field inside the membrane is negligible. We can then use Eq. (3) with  $E_p$  representing the field in a membrane, at the location of the particle, with no particle present.

The scattered power,  $P_R$ , can then be considered as the potential change one single particle can constitute on a detector. Maximizing the sensitivity hence involves maximizing  $P_R$ . Investigating Eq. (3), we find that a variation in  $\lambda$  will maximally change  $P_R$  by a factor of 4 over the range of relevant values. In order to detect small particles, the parameter to maximize is hence  $E_p$ .

This involves designing a PC membrane that supports guided resonance modes that produce high electromagnetic field intensities in the PC membrane. In theory, the obtainable field intensity is limited by how small we can make the holes [30]. However, a reduction of the hole radius has two notable consequences. It is generally followed by a narrowing of the guided resonance bandwidth, and make the resonant modes sensitive to any changes from nominal design. Imperfect periodicity or general defects can cause narrow banded resonances to disappear in practice. Secondly, as the hole radius is reduced, the PC membrane will gradually become similar to a slab with waveguiding properties. Scattered light from a particle trapped in the PC membrane, will spread over a larger area as the radius of holes is reduced. The obtainable field intensity is hence set by processing accuracy, and the guided resonance field enhancement always comes with a trade-off in imaging resolution.

In conclusion, by working at wavelengths where harmonic linearly polarized normal incidence fields couple to guided resonance modes, PC membranes can be used to produce high electromagnetic field intensities. If they are small enough, particles trapped in the membrane can then be treated as dipole sources similar to ideal dipoles. Their scattered power is then described by Eq. (3).

A dipole source placed inside a PC membrane can couple light into guided modes and can be trapped in the membrane indefinitely. However, if  $\lambda < \sqrt{2}a$ , no guided modes can exist. Light can couple into guided resonance modes, but all the scattered power from a small particle will at some point exit the membrane and can potentially be picked up by a detector on the outside of the membrane. Moreover, if the particle can be treated as a source similar to an ideal dipole, it will radiate a spherical-like wave.

Spherical waves can be refocused to spots in an imaging plane. Picturing the membrane with a microscope with backside illumination and a CCD-camera, we hence expect pixels corresponding to the location of particles to appear as bright spots when incident light couples to guided resonance modes. The contrast will be dependent on the field amplitude and phase at the location of the particle, and the amplitude and phase of the scattered light relative to the transmitted wave.

As seen from a detector outside the membrane, it is not clear that a scattering particle trapped in a PC membrane radiates spherical-like waves. The distribution of scattered irradiation from the particle will be strongly influenced by the PC membrane dimensions and particle position. Scattered irradiation can also be partially guided by the PC membrane, to be spread over a

larger area. However, we will ignore these effects for now and see how the ideal dipole model can explain the measurement results.

### 3. Fabrication and experimental setup

Standard semiconductor production techniques were used to make a thin film stack of  $\text{Si}_3\text{N}_4/\text{SiO}_2/\text{Si}_3\text{N}_4$  on 200  $\mu\text{m}$  thick silicon wafers, with double-sided polishing. A film of  $\text{Si}_3\text{N}_4$  was deposited using low pressure chemical vapor deposition (LPCVD). Next, the  $\text{SiO}_2$  film was formed by poly-Si LPCVD, followed by thermal oxidation. Finally, another film of  $\text{Si}_3\text{N}_4$  was deposited using LPCVD. Refractive index and thickness was measured with a HORIBA Jobin Yvon PZ2000 632.8 nm Laser ellipsometer and estimated by curve fitting using the least square method. Surface roughness was not measured.

A lithography step was performed to open a 700x700  $\mu\text{m}$  square in the thin film stack, on the backside of the wafer. This was done with a period of 10 mm in two dimensions before the wafer was diced into 10x10 mm chips. On the front side of the chips, E-beam lithography with a 30kV Raith150 system and reactive ion etching (RIE) with a Plasmalab System80Plus from Oxford Instruments was done to produce the PCs. The nominal design was a quadratic pattern with a hole radius of  $r = 145$  nm and a lattice period of  $a = 490$  nm.

The PC membranes were freed by etching in tetramethylammonium hydroxide (TMAH) at a temperature of 80 °C. The etch rates of Si and  $\text{Si}_3\text{N}_4$  were  $26.6 \pm 1$   $\mu\text{m}/\text{hour}$  and  $5 \pm 1$   $\text{Å}/\text{hour}$ , respectively. The total etching time was 490 min. A 39 min over etch was done to ensure that no Si was left on the backside (cavity side) of the membranes. The front side was not protected during etching. Referring to Fig. 2, layer 3 was hence etched for 490 min, and layer 1 nominally for 39 min. All chips were inspected by scanning electron microscopy (SEM). SEM imaging software was used to measure the period and radius of the PCs.

Finalized membranes were characterized using a custom built optical setup. The setup is illustrated in Fig. 3. It is comprised of a standard 35W halogen lamp, an Oriel Cornerstone 130 1/8 m Monochromator, an Olympus BX61 TRF microscope and an Olympus F-view II CCD camera. The light from the halogen source is guided via the monochromator by a set of lenses and optical fibers, to provide the microscope with collimated monochromatic back-side illumination with normal incidence and divergence 0.01 – 0.02 rad. The bandwidth of the monochromator is  $1.5 \pm 0.5$  nm. The CCD camera only sees the transmitted light, and the reflected light is discarded. The used microscope objective is an Olympus UPlanFL 40x/0.75 NA. At this magnification, one pixel on the CCD screen corresponds to  $0.16 \times 0.16$   $\mu\text{m}^2$  on the membrane surface.

### 4. Results and discussion

Processed PC membranes were free-standing in the center of 1  $\text{cm}^2$  chips. Chip and PC dimensions are illustrated in Fig. 4(A). The refractive index at 638.4 nm was measured to  $1.998 \pm 0.01$  and  $1.464 \pm 0.01$  for  $\text{Si}_3\text{N}_4$  and  $\text{SiO}_2$ , respectively. No optical quality degradation due to mechanical stresses in the thin films was observed. Stress in the  $\text{Si}_3\text{N}_4$  is tensile and will overcompensate the compressive stress in the  $\text{SiO}_2$ , stretching the membrane and preventing deformation. An incline of the hole walls and rounded edges are pointed out in Fig. 4(A). These features have not been quantified, but are to some extent unavoidable with the current methods used to free etch the membranes.

SEM images in Fig. 4(B) show a real PC membrane and reveal two defects in the PC. In the lower right corner of the image, a lattice defect that extends 2-3 periods in the vertical direction and 1.5 in the horizontal. A nano-particle with radius  $75 \pm 25$  nm has settled inside a hole shown in the lower left of Fig. 4(B). These defects were introduced non-intentionally during the fabrication process, but they are well-suited objects for preliminary studies.

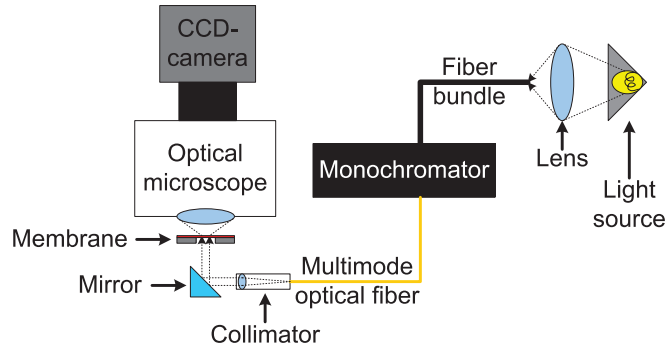


Fig. 3. A halogen light source connected to a monochromator provides the microscope with backside illumination with tunable wavelength. A photonic crystal membrane is placed in the field of view and imaged with a CCD-camera. Transmitted intensity through the membrane can hence be measured with spatial resolution, and as a function of wavelength.

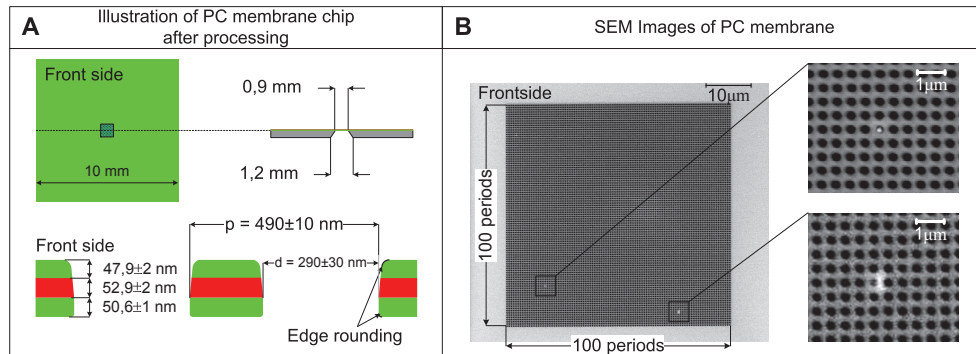


Fig. 4. (A) Illustration of photonic crystal (PC) membrane chip after processing. (B) SEM images show top views of the PC membrane. Two defects in the PC membrane have been magnified.

We have not determined the material composition of the defects, so their permittivity is not known. Based on the materials present in our fabrication facilities, it is limited to a range between 2.25 and 12.25. The lower limit is comparable to the permittivity of relevant biological target particles, which typical have a permittivity between 2 and 2.5 [36]. Using Eq. (3) and air as the surrounding media,  $\epsilon_m \approx 1$ , we can then find a relative measure of the scattered intensity from the trapped nano-particle compared to a relevant biological particle of the same size. In the worst case, the biological particle has permittivity 2, while the nano-particle trapped in the PC membrane has a permittivity of 12.25. In that case, the scattering intensity will be a factor of 10 higher for the nano-particle trapped in the PC membrane.

Images were taken with the optical setup in Fig. 3 at wavelengths between 490 and 692 nm. The set of pixels M, defined in Fig. 5, was averaged to provide a measure of the average transmittance of the PC membrane. The result is given in Fig. 6(A).

Two dips in transmission can be seen around 566 and 630 nm. They correspond to the dips found in simulations represented by Fig. 2(C) around 575 and 631 nm, and imply that the fabricated structure supports guided resonance modes. We can hence expect to have an amplification of the field inside the membrane in the spectral vicinity of wavelengths 566 and 630 nm. The difference between measured and simulated results, can be attributed to the devi-

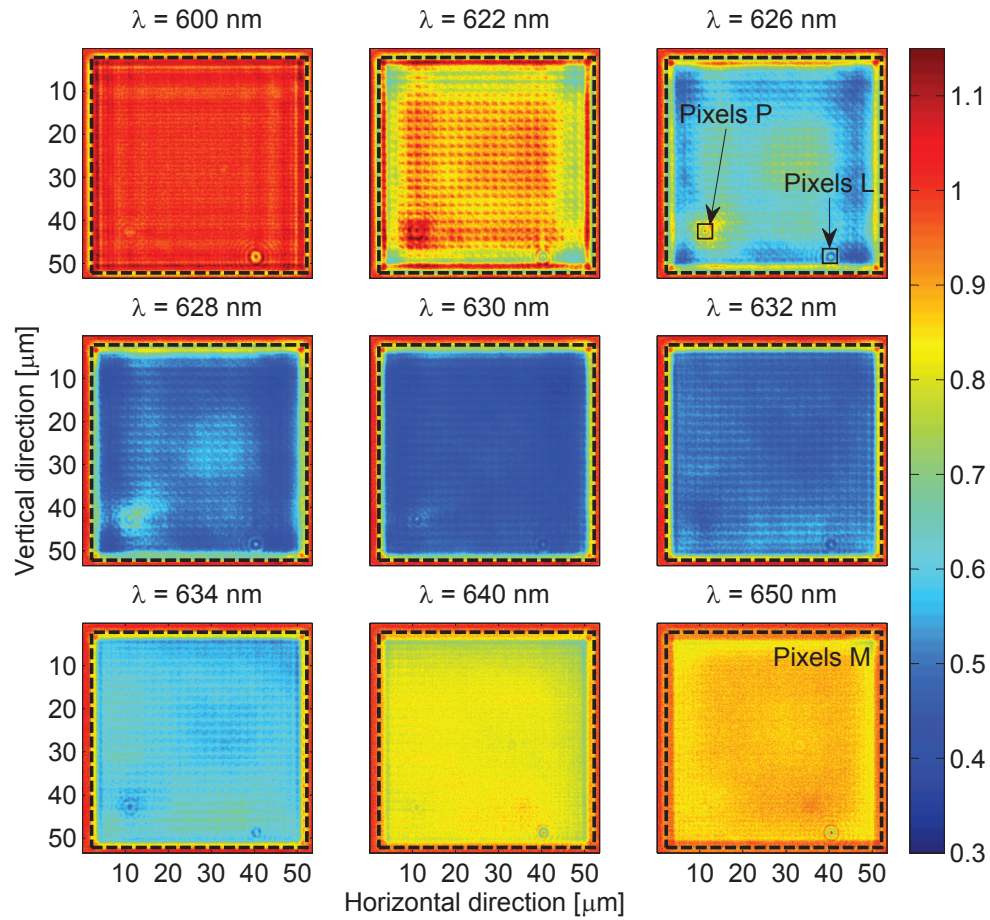


Fig. 5. Images of the PC membrane taken with the CCD camera at nine different wavelengths. The dashed black line bounds pixels M and correspond to the hole matrix. Pixels P and L are centered at pixels corresponding to the two defects in the PC membrane. The color bar shows pixel values, normalized with respect to the transmitted intensity recorded without the membrane present, at each wavelength respectively.

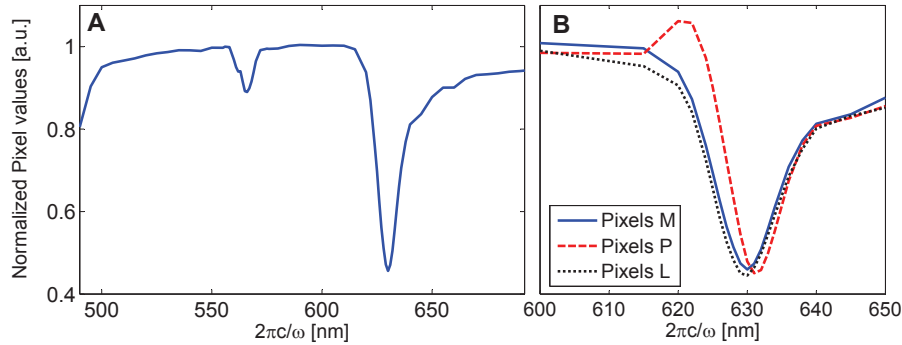


Fig. 6. (A) Average value of pixels M, defined in Fig. 5, corresponding to the transmittance of the PC membrane as a function of wavelength. (B) The average of pixels M is compared to average values of pixels P and L. Pixels P and L are also defined in Fig. 5, and correspond to the trapped nano-particle and lattice defect, respectively. Pixel values of the CCD camera have been normalized with respect to the transmitted intensity recorded without the membrane present, at each wavelength respectively.

ation from nominal thickness and inhomogeneities in hole radius and lattice period over the PC membrane, caused by limitations in fabrication accuracy. Moreover, the simulations are based on perfectly plane monochromatic incident waves. In reality, the output of monochromator has a finite bandwidth and the collimated beam a divergence. In measured transmittance, this will appear as broadening of the guided resonance bandwidths and an increase of peak values for the two dips.

From section 2.2, we then expect small particles in the membrane to show increased scattering and appear as bright spots on the CCD camera, provided that the particles are size limited by Eq. (2) and  $r_p \ll r$ , where  $r$  is the radius of holes. In this respect both the lattice defect and the nano-particle are too large, and the approximation that the field distribution in the membrane is unaffected by their presence is not necessarily correct.

Indications of the latter can be seen for the lattice defect. A selection of nine images, taken at nine different wavelengths between 600 and 650 nm, is given in Fig. 5. They show the view of the CCD camera, as the wavelength is scanned past the dip centered at  $\lambda = 630$  nm. The large lattice defect is visible on all pictures, but there is no clear indication of increased scattering as a function of coupling to guided resonance modes. To the contrary, it stands out more clearly at 600 nm, where we expect the field in the membrane not to be amplified. Its effect is also not especially large compared to its size, indicating that what we see is simply the particle being imaged. In conclusion, the behavior of the large lattice defect can not be approximated by small particle scattering theory. The analysis of the lattice defect is further complicated by the fact that it is close to the edge of the PC membrane, where the field distribution of the incident field is affected by edge effects.

The nano-particle, on the other hand, behaves very differently and clearly shows increased scattering at wavelengths where we expect the field in the membrane to rise. At 600 nm the particle is barely visible. The field in the membrane is expected to be low, and so is the scattering amplitude. Moreover, the background is maximized, inducing minimal contrast. When increasing the wavelength, we expect the light to couple to the guided resonance mode at 630 nm and the field inside the membrane to increase. The particle should start to appear as a bright spot. Indeed it does, and the contrast between the background and the spot gradually increases as the average transmittance decreases and more light couples into the guided resonance mode.

Optical characterization of the membrane has also been done in the spectral region around

the dip at 566 nm. The dip in transmittance at 566 nm is not as deep as the one at 630 nm, possibly because the 566-nm resonance is more sensitive to deviations from perfect periodicity and other defects from fabrication. Furthermore, near 566 nm we find no significant difference between the spectra of pixels M (representing the nano-particle in the PC membrane) and pixels P (representing the average transmittance of the PC membrane), so we confined our attention to the spectral region around 630 nm, where such a difference is evident.

The contrast between pixels corresponding to the location of the nano-particle and the average transmittance is given in Fig. 6(B) as a function of wavelength. The average value of pixels P, defined in Fig 5, is plotted together with the average transmittance. The frame holding the set of pixels P is centered at the location of the nano-particle. It shows how maximum contrast is reached at 626 nm. As we pass 626 nm, the contrast between the particle and the background decreases. This is counter intuitive, because we expect the field intensity in the membrane to peak closer to 630 nm. However, the observation can be explained as follows: For normal incident light and  $\lambda > a$ , the optical response is particularly simple. The sum of sources from each unit cell of the membrane produce a transmitted field that is bound to the 0<sup>th</sup> order of diffraction. It can be defined with an amplitude and a phase. Treating the nano-particle with small particle scattering theory, we can imagine that it radiates like a dipole. It also has an amplitude and a phase. The contrast is hence not only dependent on amplitude, but also on phase. The phase of the dipole should be the same as the guided resonance mode field at the specific location of the particle. Considering how the phase of the mode field at that location is in general different from the phase of the mode field average over the unit cell, we do not expect there to be a one-one relation between contrast and the amplitude of the guided resonance mode field.

Finally, we note that the molecules we are interested in detecting are found in liquid samples as blood, saliva, urine, etc. In biosensing it is hence most relevant to focus on detection of nano-particles in water. The current PC membrane has been design for detecting nano-particles in air, and the consequence of using the current sensor in water is considerable. The permittivity in the material surrounding the PC membrane then increases to  $\sim 1.7$  for visible light [38], and will in general completely change the spectral response of the PC membrane. In order to ensure field enhancement through coupling of incident light into guided resonance modes, the membrane and lattice geometries will need to be redesigned. Moreover, the scattered intensity from nano-particles in the Rayleigh regime is proportional to the permittivity contrast between the scattering particle and the surrounding material squared,  $|\epsilon_p - \epsilon_m|^2$ . Increasing  $\epsilon_m$  will hence lead to a reduction in scattered intensity. In conclusion, adapting the sensor to detect nano-particles in water will require a change in membrane geometries, and will to some degree reduce the sensitivity.

## 5. Conclusion

The current system can easily detect and spatially locate single particles with radius down to 75 nm in air. Our measurements indicate that detection is a result of amplified small particle scattering, provided by coupling of the incident light to guided resonance mode fields supported by the PC membrane. This is a useful effect, because in that case, each hole in the membrane can effectively work as a sensor for single nano-particles, and the large number of holes ensures a great dynamic range. As described in the section above, we also see the potential for designing PC membranes for detection of particles in water-based solutions.

The sensor is based on small particle scattering, so the sensitivity can be increased by producing PC membranes supporting resonant modes that produce high electromagnetic field intensities in the PC membrane. This is attainable since field intensities produced by resonant modes are in theory only limited by how small we can make the holes [30], and production techniques continue to reach new levels of accuracy. That said, field enhancement through coupling to

guided resonance modes always comes with a trade-off in image resolution. The latter issue has not been investigated in detail. It is considered a topic for further research, but will effect the dynamic range of the sensor. It can also effect the contrast, since the scattering amplitude of the particle, as seen from a detector outside the membrane, will be reduced as the scattered power spreads over a larger area.

As it stands today, the sensor is not a biosensor, but the membrane is designed to be used in one. The complex geometry of the thin stack arranges for chemical passivation of the  $\text{Si}_3\text{N}_4$  surface, while the  $\text{SiO}_2$  inside of holes can be functionalized to capture specific bio-molecules. Target molecules will settle at positions of maximum optical field intensity, ensuring maximal sensitivity. Furthermore, the large number of holes provides a means for efficient processing of large samples. Pushing samples through the membrane instead of flushing them over, has been shown to be an efficient way of making particles in the sample interact with the membrane surface [37]. Since a target molecule has to touch a functionalized surface in order to be captured, through holes enhance the likelihood of target capture.